Investigating the reaction mechanism of zirconium as a fuel in reactive multilayer films via multimodal analysis

Vidushi Singh, Tao Wu, Christophe Tenailleau, Teresa Hungria, Alain Estève, Carole Rossi

Chemical Engineering Journal 495 (2024) 153357

Contents lists available at ScienceDirect

Chemical Engineering Journal

journal homepage: www.elsevier.com/locate/cej

Investigating the reaction mechanism of zirconium as a fuel in reactive multilayer films via multimodal analysis

Vidushi Singh [a], Tao Wu [a], Christophe Tenailleau [b], Teresa Hungria [c], Alain Estève [a], Carole Rossi [a,*]

[a] LAAS-CNRS, University of Toulouse, 7 Avenue du Colonel Roche, 31400 Toulouse, France
[b] CIRIMAT, CNRS, Universite Toulouse 3 - Paul Sabatier, 118 Route de Narbonne, 31062 Toulouse Cedex 9, France
[c] Centre de Microcaractérisation Raimond Castaing, 3 Rue Caroline Aigle, 31400 Toulouse, France

ARTICLE INFO

Keywords:
Thin-films
Sputtering
Energetic material
Nanolaminates
Zirconium

ABSTRACT

In this report, we examine the intricate details of the mechanism driving Zr/CuO thermite system, shedding new light on the exceptional reactivity of Zr fuel with oxygen. Magnetron-sputtered Zr/CuO reactive multilayers were deposited, and thermo-physical techniques were employed to characterize the progression of the chemical reaction upon heating. Unlike commonly used Al fuel, Zr/CuO exhibited 100% heat release below 500 °C, contrasting with the ~5% observed for conventional Al/CuO system. This enhanced reactivity at low temperature is attributed to the rapid oxygen consumption behavior of Zr, due to the poor barrier of ZrO_x to oxygen diffusion. The oxidizing behavior of Zr was quantitatively analyzed using electron microscopy and spectroscopy. Our observations reveal a three-step process of Zr oxidation facilitated by a rapid reduction of CuO to metallic Cu accompanied by the formation of an intermediate Cu_2O phase: (i) a preliminary low-temperature mass transport initiating at 275 °C, (ii) partial Zr oxidation forming ZrO_2 and oxygen enriched Zr and finally (iii) complete conversion to zirconia at 450 °C. Finally, Zr/CuO reactive thin-films demonstrated a very high reactivity with an ignition delay time of 0.04 ± 0.016 ms and a burn rate of 3.5 $m.s^{-1}$, in stark contrast to the same volume of Al/CuO, which failed to ignite and burn altogether. This study not only deepens our comprehension of Zr-based thermite system but also underscores its potential for diverse applications in energetic materials.

1. Introduction

Energetic materials (EMs), capable of rapidly releasing substantial amounts of chemical energy in the form of heat during combustion have been utilized for centuries to perform high-energy functions such as propulsion and demolition. Over the past two decades, the availability of metallic nanopowder has significantly facilitated the development of metal-based energetic composites. These composites, combining a metallic fuel with an oxygen source, have attracted considerable attention for their enhanced energy potential compared to conventional EMs [1]. This enables high energy outputs within a reduced volume opening up to new fields of applications such as thermal batteries for power generation [2], energy supplies for outer space applications [3], self-destructing microchips [4,5], pipe welding in geothermal power plants or plugging in harsh environments [6]. The widespread availability and high volumetric and gravimetric energy density of aluminum (Al) make it one of the most extensively utilized metallic fuels in metal-based energetic composites [7,8]. But, its native alumina (Al_2O_3) penalizes its ignitability. Due to its high oxidation enthalpy (78.1 kJ. cm^{-3}), strong affinity with oxygen [9], zirconium (Zr) is also an excellent metallic fuel already used in high-energy propellants [10,11]. As an example, zirconium–potassium perchlorate (ZPP) is widely employed in the NASA Standard Initiator to ignite various pyrotechnic systems. It yields rapid pressure rise, generates minimal gas, emits hot particles when ignited, maintains thermal stability, possesses a long shelf life, and remains stable under vacuum. However, its susceptibility to electrostatic discharge discourages a wider use of Zr as a fuel [12], especially in the traditionally employed powder form. Several efforts have been dedicated to passivate the metal surface to prevent unwanted reactions, Fe_2O_3 being most commonly used [13,14] both as a surface coating and an oxidizer for combustion. While Zr's usefulness for ignition applications is well established, its use as a fuel in thermite reactions is relatively unexplored. In a recent endeavor to produce highly reactive nanocomposites, metallic Zr was introduced into aluminized

* Corresponding author at: LAAS-CNRS, 7, Avenue du Colonel Roche, 31400 Toulouse, France.
E-mail address: carole.rossi@laas.fr (C. Rossi).

https://doi.org/10.1016/j.cej.2024.153357
Received 3 May 2024; Received in revised form 6 June 2024; Accepted 19 June 2024
Available online 20 June 2024

nanothermites, resulting in a notable enhancement in reactivity [15]. This result was confirmed in a study conducted on Al:Zr/TiO_2 composites for welding, revealing decreased ignition temperature and higher reactivity compared to the Al:TiO_2 baseline sample. This enhancement was attributed to the opening up of multiple channels of heat transfer resulting from the intermetallic reaction prior to the thermite reaction. However, no fundamental research work has studied the reaction mechanisms of Zr when in contact with a metallic oxidizer. Mily et al. [16] conducted a comprehensive comparison of various M/CuO (M: Al, Mg, Zr) thermite composites regarding their reactivity, but detailed insights into the sequential stages of the chemical transformation between Zr and CuO were not covered.

The objective of this work is twofold. First, it aims at elucidating the reaction mechanisms involved in the reaction of Zr in contact with a strong metallic oxidizer like copper oxide (CuO). For that purpose, we produce high purity and well-defined Zr/CuO nanothermite and analyze the oxidation sequences upon annealing in neutral environment. Magnetron sputtering technique was chosen to produce Zr/CuO samples as it permits a very well controlled interface (in thickness and structure) between the fuel and the oxidizer. This provides an ideal model-system to quantitatively describe the interfacial oxide (ZrO_x) growth and microstructural evolution upon heating. Furthermore, preparing Zr/CuO samples by sputtering, we ensure the absence of native oxide shells on the Zr layer due to the high vacuum process, enabling us to probe the early oxidation stages. A second objective is to investigate the ignitability and the capacity for self-propagation of Zr-based thermite.

Interestingly, the results revealed that CuO undergoes a rapid reduction to metallic Cu at remarkably low temperatures of ~275 °C. An intermediate Cu_2O phase was detected only at this low temperature, but it was not observed in further characterization at the interfaces. Subsequently, oxygen diffuses across the Zr/CuO interfaces, initiating the oxidation of Zr at ~240 °C. This contrasts starkly with the behavior of Al, where such low temperatures primarily facilitate dual Al-O diffusion [17]. Moreover, we highlighted that the formation of a zirconia layer promotes oxygen transport to the metallic Zr core, facilitated by its higher oxygen diffusivity (2.41×10^{-11} cm^2/s), whereas amorphous alumina acts as a hindrance to oxygen transport. Consequently, the thermite system is prompted to enter a self-sustaining reaction state, driven by the abundant energy available to initiate a greater degree of mass transport across the continually evolving zirconia layer oxide until the reaction concludes at approximately 450 °C. The dominance in the reactive behavior of Zr is also evident in the ignition and combustion properties compared to Al.

2. Materials and methods

2.1. Reactive multilayer films preparation

Nanolayers of Al, Zr and CuO were fabricated through Direct Current (D.C.) magnetron sputtering. An 8 by 3 by 0.25 in. Zr target (99.95 %) and Al target (99.99 %) from Neyco, France, and an equivalently sized Cu target (99.999 %) from Codex, France, were utilized for the deposition in an equipment from Thin Films Equipment (TFE), Italy. Each nanolayer, controlled by a prior calibrating process, was deposited at a base pressure of 1.5×10^{-7} Torr. The Ar gas flow was set to 82 s.c.c.m. for Zr; while the O and Ar gas flows for CuO were maintained at 16 s.c.c.m. and 32 s.c.c.m., resulting in the deposition pressure for the two nanolayers to be 13 mTorr and 8 mTorr respectively. The sputtering powers for Zr and CuO depositions were set to 200 W and 600 W respectively. The unbiased sample holder was placed 15 mm away from the target. Following the deposition of each nanolayer, the sample holder was cooled down under Ar for a set time.

Several configurations of the reactive multilayer films were prepared for testing ignitability, material sensitivity and performing thermochemical analysis. To fabricate ignition chips, 3-bilayers (BL) of Zr/CuO were deposited on 4-inch 525 μm-thick eagle XG standard glass wafers, which were pre-processed using optical photolithography to define the Ti resistive element as well as the Au contact pads. The detailed manufacturing process can be found in our previous works [18,19]. The thicknesses of each of the two nanoscale films, CuO, and Zr, were set to 200 nm and 220 nm, respectively, following an equivalence ratio of 2. For comparison purpose, ignition chips with 3-BL of Al/CuO were also fabricated following the same process and conditions, with the exception that the thickness of the Al nanolayer is set at 200 nm to maintain an equivalence ratio of 2.

The thermochemical analysis, autoignition-temperature as well as combustion tests were carried out using free-standing foils of 3 BL of Zr/CuO prepared using a simple lift-off technique [19,20]. In addition, 3 BL of Zr/CuO were also deposited on a standard 4-inch Si substrate to perform chemical analysis upon annealing. It is important to note that throughout this manuscript, the deposition order is described in ascending order, with each layer separated by a hyphen.

2.2. Material characterization

Thin-film structural determination on each nanolayer as well as the annealed samples was conducted using a SIEFERT XRD 3000 TT X-Ray diffractometer equipped with Cu-Kα radiation ($\lambda = 1.5406$ Å) and fitted with a diffracted beam graphite monochromator. X-Ray Diffraction (XRD) measurements were performed in the 2θ range of 10° to 60° with a step size of 0.04°. FEI Helios NanoLab DualBeam FIB-SEM was used to study the morphology as well as perform a Focused Ion Beam (FIB) technique to prepare cross-sectional lamellae. The physio-chemical transformation of the multilayers was analyzed using Transmission Electron Microscopy (TEM) using a JEOL cold-FEG JEM-ARM200F operated at 200 kV equipped with a prove Cs corrector reaching a spatial resolution of 0.078 nm. Electron Energy Loss Spectroscopy (EELS) data were acquired on a Gatan imaging filter quantum (energy resolution of 0.3 eV) using a dispersion of 1 eV/channel, a collection angle of 29.4 mradians and a semi-convergence angle of 14.8 mradians. The spatial resolution was estimated at 0.5 nm. Energy dispersive X-ray (EDX) spectra were recorded on a JEOL CENTURIO SDD detector.

The heat released during each chemical reaction step in the multilayers was assessed through thermal analysis. This analysis was conducted in an Ar atmosphere using Differential Scanning Calorimetry (DSC) with a NETZSCH DSC 404 F3 Pegasus system. Equipped with a DSC-Cp sensor type S and a Platinum furnace, the system recorded diffractograms normalized to a typical foil mass of ~10 mg. Heating proceeded at a constant rate of 10 °C/min until 950 °C, with subsequent manual baseline adjustment.

Slow annealing experiments were performed in a high-metals tube furnace (AET Technologies) under an inert N_2 atmosphere. The heating rate matched the DSC's rate at 10 °C/min, followed by a cooling rate of 2 °C/min.

2.3. Characterization of the energetic properties

The auto-ignition temperature, defined as the temperature at which the thermite ignites spontaneously, was determined using hot-plate tests. Approximately 2 mg of free-standing foils were brought into a direct contact with the pre-set surface of the hotplate, and the temperature was determined by observing a flash. The foil specimen was dropped on the hot-plate surface once the temperature fully stabilized.

The ignition energy is determine using the temporal integral of power upto the event of initiation averaged over several ignition tests. Each chip is resistively heated keeping the dissipated power at 6.125 W and the photocurrent is detected using an externally biased photodiode (5 V, VISHAY, BPV10) placed a few centimeters away from the sample. The signals were acquired using an oscilloscope, and subsequent data processing was performed using in-house programs.

The propagation rate was determined using a high-speed camera (VEO710, Phantom, USA) recording at 48,000 frames per second with a

resolution of 512 × 64 pixels. The recorded videos from multiple samples of each type were analyzed using Phantom Camera Control (PCC) Software. Briefly, six two-point measurements were conducted to determine the propagation speed for each device across all the thermite configurations. Subsequently, the macroscopic burn rate was calculated as the mathematical average for each multilayer.

3. Results and discussion

3.1. Nature and structure of interfacial layers

To understand the mechanisms underlying the reactions in Zr/CuO multilayers, thought to be primarily controlled by the outward migration of oxygen atoms from the CuO matrix towards the Zr layers via interfacial layers, it is imperative to accurately characterize the CuO and interfacial domains as an initial crucial step. For that purpose, CuO-Zr-CuO-Al multilayer stack was deposited onto a Si wafer and characterized using scanning transmission electron microscopy coupled with EELS (STEM-EELS) in its as deposited state.

A representative STEM image of the full stack as well as the TEM micrographs of each interface are shown in Fig. 1**a** and Fig. 1**c-e**. The corresponding EDX profile across an ascending line scan is shown in Fig. 1**b**. We distinguish between the CuO-Zr interface, formed by depositing Zr onto CuO layer from the Zr-CuO interface, formed by depositing the CuO layer onto a Zr layer. An Al top layer is added as a capping layer and also serves for comparison purposes. Images are acquired in High Angle Annular Dark Field (HAADF) – STEM mode. HAADF imaging is an incoherent mode of imaging whereby the image contrast is approximately proportional to the atomic number ($\sim Z^2$) of the constituent atoms due to Rutherford-like scattering [21].

The thickness of each layer, CuO_{bottom}, Zr, CuO_{top} and Al are 192 ± 2.5 nm, 226 ± 6.2 nm, 203 ± 6.9 nm and 206 ± 13.3 nm. The CuO layers, as shown in Fig. 1**a**, are clearly polycrystalline, displaying a coarsened morphology consisting of disordered columnar grains, which aligns with previous observations in sputtered thin films [22,23]. The Zr layers, as depicted in Fig. 1**a**, display a granular morphology as reported previously [24], with each column oriented in various directions, likely influenced by the rough CuO surface and its jaggedness. An EDX linescan quantifying the presence of Zr and O is shown in **Figure S1** in the **Supporting Information**. The obvious optical contrast clearly demarcates each of the three interfaces, CuO-Zr, Zr-CuO and CuO-Al. Their respective thicknesses measure 10 ± 1.1 nm, 14 ± 2.8 nm and 6 ± 1.2 nm. The roughness of the surface of the CuO layer results in a dense but uneven CuO-Zr interface. The resulting growth of Zr columns in turn causes the formation of an irregular Zr-CuO interface. Even though the interfacial boundary is asymmetrical, the interface is dense and presents no voids or major physical defects. Fig. 1**b** shows the CuO-Zr-CuO-Al stack mapped using EDX for Cu, O, Al and Zr, depicting severe Cu-O-Zr elemental intermixing at each of the two Zr/CuO interfaces. Excess oxygen observed at each of the three interfaces may stem from the inherent properties of the metals or from the oxygen plasma present in the sputtering chamber during successive depositions, resulting in slight oxidation of the metals. Specifically, for Zr, this can also arise from its materialistic property of high oxygen solubility [9], which in turn starts a chemical reaction in the close proximity of the interfaces. Quite expectedly, most of the oxygen is concentrated at the two extremums of the metallic Zr layer, at its interfaces with CuO. The darker regions at the interfaces are comprised of O, Cu and Zr, as shown in the EDX map in **Figure S2** in the **Supporting Information**, confirming the initiation of Zr oxidation. The quantification at the interface reveals ~50% Cu, ~30% O and ~20% Zr (**Figure S3**, **Supporting Information**). Additionally, an EDX quantification of contrasting regions of the bottom CuO layer reveals ~84% Cu and 16% O in the darker regions against 67% Cu and 33% O in the lighter regions of CuO, close to the interface (**Figure S4**, **Supporting Information**). Due to the low mass of oxygen, EDX may not be the most accurate method for quantifying its presence,

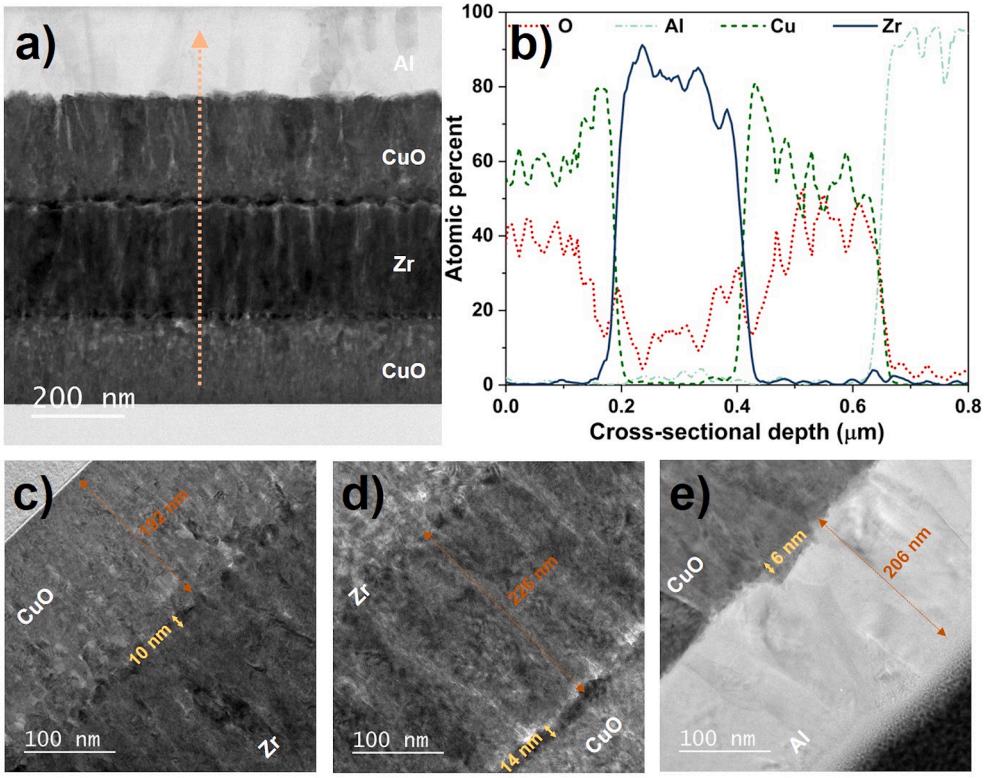

Fig. 1. Pre-anneal microstructure of CuO-Zr-CuO-Al multilayer, showing: **a)** STEM micrograph of the CuO-Zr-CuO-Al and **b)** corresponding EDX quantification of O, Cu, Al, and Zr. Additionally, TEM micrographs depicting each of the three interfaces: **c)** CuO-Zr, **d)** Zr-CuO, and **e)** CuO-Al.

but it offers a valuable qualitative evaluation critical to the quantitative analysis. EELS, on the other hand, confirms the change in the oxidation state of Cu from + 2 (in CuO) to + 1 (Cu_2O), depicted by a shift in L edge from 931 eV to 933 eV [25] (**Figure S5, Supporting Information**). Such an initiation of the Zr oxidation in the vicinity of the interface is another indication of a high reactivity of Zr. Finally, CuO-Al interface is characterized by dense non-uniform edge mainly comprised of alumina similar to the observations in the previous reports [20,22]. These initial characterizations highlight the oxygen scavenging behavior of Zr against Al. Subsequently, the respective reactivities of Zr/CuO against Al/CuO are investigated.

3.2. Thermo-physical analysis

The DSC analysis involved examining the reaction sequences of Zr/CuO and Al/CuO foils at slow heating rates (10 °C/min) in an oxygen-free environment. The total heat of reaction was determined by integrating the exothermic peaks over time within the 200 – 950 °C range and normalizing the values with respect to the foil mass, as indicated across each plot. To supplement the understanding of the different reaction steps, Zr/CuO sample was annealed in an oxygen-free environment at 275 °C, 375 °C, 450 °C and 950 °C corresponding to the main peaks recorded in the DSC scan and their respective compositions were analyzed by XRD. The XRD diagrams can be found in **Figure S6, Supplementary Information** and the composition after annealing steps is summarized in Table 1.

While the total heats of reaction for CuO/Zr and CuO/Al are remarkably similar (approximately 1.250 $kJ.g^{-1}$), significant differences in the occurrence of exotherms can be observed in Fig. 2. In Zr/CuO, the reaction onset occurs at temperatures as low as 275 °C, compared to 395 °C for Al/CuO, and it takes place in the solid phase, below 500 °C, in a two-step reaction. The first weak exotherm is centered at ~300 °C (onset ~240 °C) followed by a second strong exotherm at ~410 °C. Notably, there is no heat released upon the completion of the second exotherm, unlike Al/CuO, which exhibits an exotherm at approximately 800 °C after the Al melting as reported previously [22].

The initial event at ~300 °C corresponds to the initial oxidation of Zr facilitated by outward oxygen migration from CuO. Cu_2O, ZrO and ZrO_2 are detected in the XRD at 275 °C. Such reaction, accompanied by only weak heat release, can only come from the preliminary atomic mass transport of O across the native interfaces (~10–14 nm in thickness), facilitated by the strong oxygen affinity of Zr, as well as the capability of oxygen to migrate into the interstitial sites of the Zr metal lattice [9]. This oxidation process rapidly saturates Zr with oxygen, leading to the reduction of CuO. It is interesting to note that the first appearance of Cu is seen in the XRD at ~375 °C, which is at the completion temperature of the first exotherm which releases approximately 20% of the total heat. Similar occurrences have been previously reported within a comparable temperature range [16]. It has to be noted that following the completion of the first exotherm at ~375 °C, a significant presence of ZrO_2 and Cu is detected. The presence of CuO remaining in the sample suggests that the complete CuO decomposition into Cu occurs predominantly close to the Zr fuel. This will be further analyzed by STEM-EELS. No Cu-Zr intermetallic formations are detected in the system at any temperature, meaning that Zr-O bond formation is favored over Zr-Cu. Besides, a low oxidation temperature precludes metallic bond formation between Cu and Zr. Following the final exothermic event, which concludes around ~475 °C, the product showed the presence of ZrO_2 and Cu indicating the complete Zr oxidation through CuO decomposition. Subsequent to this temperature until reaching 950 °C, no further changes were observed except for a stronger presence of ZrO_2 in the diffractogram. It is noteworthy that the XRD analysis of the sample annealed at 950 °C displayed improved signal strength due to its powdered form, unlike the thin-film nature of the other samples. Upon revisiting the reference Al/CuO system, Cu_2O was observed to persist at approximately 500 °C [20,22], suggesting that the kinetics of CuO reduction is accelerated in the presence of Zr compared to Al. This observation is consistent with the documented effect of refractory metals like Zr, which notably facilitate the kinetic enhancement of the CuO reduction reaction, as reported in [26].

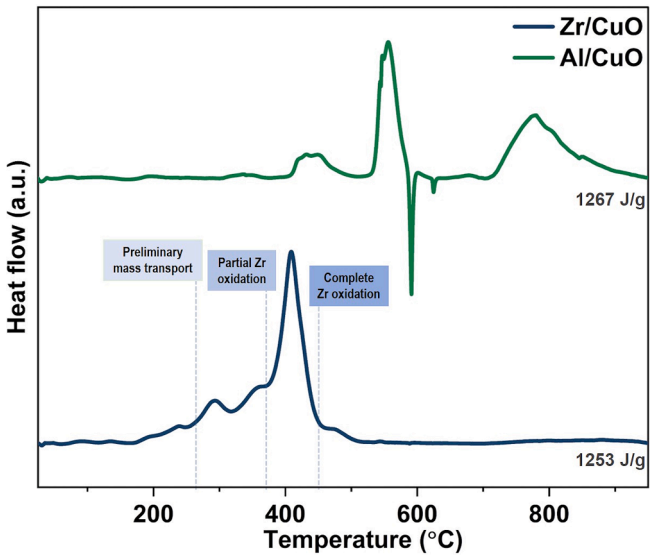

Fig. 2. DSC traces of 3 BL Zr/CuO and Al/CuO. The three key temperatures, representing critical transformation regions of preliminary mass transport, partial and complete Zr oxidation, are marked against the Zr/CuO plot.

It is interesting to note that the actual heat released is significantly lower than the theoretical values (Table 2), with Zr/CuO and Al/CuO samples exhibiting 55% and 36%, respectively. However, the higher ratio achieved with Zr/CuO is likely due to the rapid and low-temperature oxidation of Zr. This eliminates intermediary reactions, such as intermetallic reactions, which can affect the overall reaction yield. In contrast, during the Al/CuO reaction, intermediary reactions leading to the formation of Al_xCu_y products and suboxides were observed [27].

In summary, thermo-physical analysis of the Zr/CuO system points to its superior reactivity over Al/CuO. The high oxygen affinity of Zr compared to Al, along with nearly 8 orders of magnitude higher oxygen diffusivity in zirconia compared to alumina, facilitates increased oxygen transport and higher heat generation. Furthermore, a higher bond dissociation energy of Zr-O bond (760 $kJ.mol^{-1}$) against that of Al-O bond (512 $kJ.mol^{-1}$) supports this claim. In order to better understand the dynamics of the Zr-CuO solid-sate reaction, CuO-Zr-CuO-Al stack was deposited on a Si substrate and characterized using STEM and EELS after being annealed at 275 °C, 375 °C and 450 °C, corresponding to the three key temperatures marking the onset of oxygen diffusion at

Table 1
Summary of constituents of 3 BL Zr/CuO multilayer stack post-anneal.

Sample	Constituents after annealing at various temperatures				
	AD	275 °C	375 °C	450 °C	950 °C
Zr/CuO	Zr, CuO	Zr, ZrO, ZrO_2, CuO, Cu_2O	ZrO_2, CuO, Cu	ZrO_2, Cu	ZrO_2, Cu

Table 2
Summary of heats of reaction of Zr/CuO and Al/CuO multilayer films.

Sample	Experimental heat (ΔH)	Theoretical heat (ΔH_{th})	($\Delta H/\Delta H_{th}$)
Al/CuO	1253	3460	0.36
Zr/CuO	1267	2314	0.55

~275 °C, oxidation of most of the Zr layer to ZrO_x around ~375 °C and finally, complete redox reaction resulting in the formation of Cu and terminal oxide around ~450 °C, as indicated by the exothermic responses observed in DSC (Fig. 2).

3.3. Reaction progression and chemical transformation

The changes in the layer, post-annealing at 275 °C, 375 °C, and 450 °C, along with the interface thicknesses at the different temperatures, are summarized in Table 3.

Preliminary mass transport: Fig. 3**a** show the STEM micrograph of CuO-Zr-CuO-Al multilayer annealed at 275 °C. The three interfaces, CuO-Zr, Zr-CuO and CuO-Al, are presented in Fig. 3**c-e** respectively. Compared the as-deposited multilayer structure, whereas both bottom and top CuO show a 10–12 % reduction in their respective thicknesses, the Zr layer decreases by a mere 8 % to about 204 ± 8.1 nm from an initial 220 nm. Additionally, the CuO-Zr interfaces grows by 350 % to ~45 nm while the Zr-CuO interface shows a 357 % increment to 64 nm. A higher degree of unevenness at the as-deposited Zr-CuO interface results into a thicker interface post anneal in comparison to CuO-Zr interface. As reported previously, the roughness of the underlying layers sets a precedent for the jaggedness of the subsequent interfaces [22]. As for the CuO-Al interface, no significant interface growth is expected in this temperature range, clear from a slight change from 6 to 7 nm, and no reduction in Al thickness.

The most striking observation is the formation of metallic Cu grains (white dotted arrows, Fig. 3**c-d** and Fig. S7**a**) at the interfaces as a result of preliminary mass diffusion across the interfaces causing Zr-CuO oxidation–reduction reaction. The initial heating to 275 °C provides enough activation energy to initiate the oxygen transport from CuO towards Zr, which rapidly oxidizes the Zr layer in the immediate vicinity. As a result, numerous voids are formed at both the CuO-Zr and Zr-CuO interfaces (dotted circular regions, Fig. 3**c-d**), alongside the emergence of metallic Cu grains throughout the interface junction between the two nanolayers. This effectively severs the close contact between the fuel and the oxidizer, essentially marking the end of primary interfacial mass transport that initiates the reaction. Meanwhile, the oxygen contained within the voids is absorbed by the Zr layer as a result of which it begins to develop a columnar morphology.

The corresponding EDX quantification ascending from the bottom CuO nanolayer to Al is shown in Fig. 3**b**. Unlike afar from the CuO-Zr and Zr-CuO interfaces wherein the average atomic ratio of Cu to O is ~1 (CuO layer), the presence of oxygen drops to ~5% (atomic percent) at the ~45 and ~64 nm thick interfaces. No simultaneous presence of Cu and Zr are detected at the interface junction indicating no intermixing between the two metals. The zirconia-Cu interlayer effectively separates the CuO and Zr at both top and bottom interfaces as shown in **Figure S8** and **Figure S9**. Zr layer shows the maximum presence of oxygen (35–40%) closer to its interfaces with CuO, and < 20% in the remaining layer. This indicates the beginning of formation of zirconia, as well as the possible storage of oxygen in the rest of the Zr layer (interstitial oxygen) **(**Fig. S7**b** and **Figure S10)**. The contrast in the Zr layer (Fig. 3**a**) is indicative of oxygen content, where low density region appears lighter and possess a higher amount of oxygen (Fig. S8**c**). The CuO-Al interface, detailed in a previous paper [22], is characterized of Al-Cu-O intermixing at the interface, but no significant chemical microstructural change at this temperature. This intermixing comes as a result of dual diffusion of Al and O atoms, which is highly dependent on the initial roughness of the interface between them. Additionally, no Al diffusion is seen throughout the rest of the multilayer thickness.

Partial Zr oxidation: Fig. 4**a-b** show the STEM image of CuO-Zr-CuO-Al multilayer annealed at 375 °C and its corresponding EDX profile recorded vertically from the bottom CuO to Al. The parallel mapping of the elements across the two CuO-Zr and Zr-CuO interfaces is shown in **Figure S12** and **Figure S13**. Whereas the bottom CuO reduces by ~22% to 156 ± 25.8 nm, the top CuO depreciates by about 29% to 142 ± 3.2 nm. Quite strikingly, Zr layer thickens to 320 ± 3.5 nm, a 44% increase compared to the initial thickness. Al layer only reduces by about 6% to 188 ± 6.3 nm as a result of its contribution to the interface thickening. Fig. 4**c-e** display a close-up view of the Zr layer and its two corresponding interfaces within the multilayer stack. Unlike previously, the CuO-Zr and Zr-CuO interfaces are dense and quite homogeneous, in addition to presenting no defects or void formation. Therefore, a conclusive measurement couldn't be obtained in each of the two cases. CuO-Al interfaces on the other hand exhibits a clear formation of ~15 nm thick amorphous alumina (Fig. 4**e**) formed as a result of Al-O diffusion cross the interface.

Annealing at 375 °C (end of first exotherm, Fig. 2) marks the beginning of Zr-CuO redox reaction resulting in the formation of terminal products Cu and ZrO_x. Fig. 4**a** clearly shows large Cu grains decorating the CuO-Zr and Zr-CuO interfaces (darker regions). Their presence reduces the contact surface area between the oxidizing Zr layer and the remaining CuO effectively marking the end of the partial Zr oxidation event. Indeed, XRD analysis at this stage indicated a very strong presence of ZrO_2 as well as that of Cu (**Figure S6**). EDX quantification supports this claim showing only about 20% oxygen content in the bottom CuO and ~30% in the top CuO layer. The absence of Cu_2O in the XRD analysis, a compound typically observed in thermite reactions involving Al and CuO, suggests that the Zr-CuO reaction proceeds differently, completely reducing CuO to metallic Cu. This contrasts with the reaction involving Al, where CuO undergoes a two-step reduction process to form Cu_2O before reducing further to metallic Cu [20,22]. Zr possess a growing columnar morphology with O present throughout the entire thickness of the layer. However, the most remarkable observation is the substantial increase in Zr concentration halfway through its thickness (**Figure S11** and **Figure S14**), coinciding with a significant decrease in oxygen concentration from an average of 40 atomic percent to nearly 25 atomic percent (Fig. 4**b**). The contrast in the STEM image supports this quantification analysis: since Zr (6.51 $g.cm^{-3}$) has a higher density than zirconia (5.68 $g.cm^{-3}$), it presents itself darker than the surrounding area as indicated by the dotted rectangular region (Fig. 4**a**). The consistency of a two-way inwards oxidation of Zr via the top and the bottom CuO is noteworthy. Given the exceptionally high melting point of Zr (1855 °C), it is challenging to justify its outward diffusion towards CuO. However, the significantly high oxygen solubility in Zr, as discussed in the previous section, supports the argument for inward oxygen diffusion, followed by the outward expansion of zirconia. The average Zr-O atomic ratio remains at 1 throughout the layer, except for the middle region, suggesting the potential formation of ZrO, which is typically regarded as an unstable oxide of Zr. Given the detection limits of EDX, it is impossible to comment on the oxidation state of Zr, however it does indicate that Zr has been only partially oxidized. This oxidation regime is highly unlike Al/CuO, wherein such low temperatures only support preliminary Al-O diffusion and interface thickening resulting in the formation of alumina. The slight presence of oxygen in the Al layer, being less than 10% seems to be only a background signal. These observations strongly support the superior reactivity of Zr as a fuel against

Table 3
Summary of thicknesses of each of the three nanolayers as well as their interfaces at various temperatures.

Layer/Interface	Thicknesses (nm)			
	25 °C	275 °C	375 °C	450 °C
Layer				
CuO (bottom)	192 ± 2.5	176 ± 5.9	142 ± 3.2	108 ± 25.5
Zr	226 ± 6.2	204 ± 8.1	320 ± 3.5	340 ± 5.2
CuO (top)	203 ± 6.9	181 ± 16.0	156 ± 25.8	150 ± 13.8
Al	206 ± 13.3	199 ± 3.6	188 ± 6.3	177 ± 12.8
Interfaces				
CuO-Zr	10 ± 1.1	45 ± 2.0	–	–
Zr-CuO	14 ± 2.8	64 ± 12.1	–	–
CuO-Al	6 ± 1.2	7 ± 1.2	15 ± 4.3	48 ± 4.4

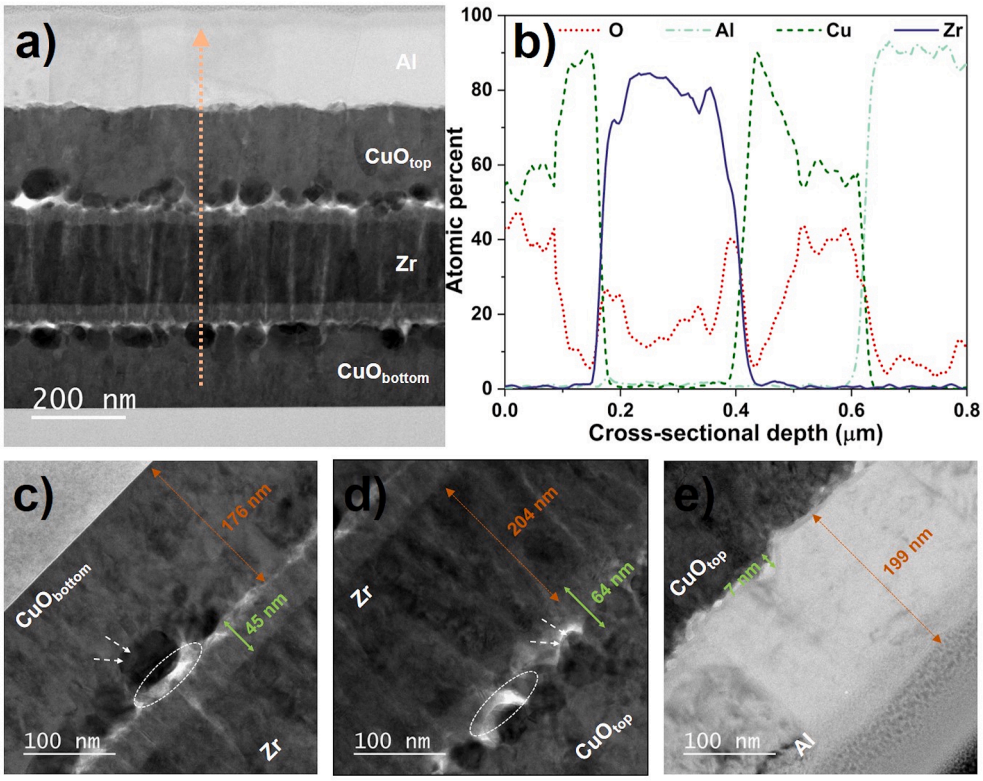

Fig. 3. Post-anneal microstructural evolution at 275 °C, featuring: **a)** STEM micrograph of the CuO-Zr-CuO-Al system and **b)** corresponding EDX quantification of O, Cu, Al, and Zr. Additionally, TEM micrographs depicting each of the three interfaces: **c)** CuO-Zr, **d)** Zr-CuO, and **e)** CuO-Al. In (b) and (c), the white dotted arrows indicate metallic Cu while dotted circular regions highlight the formation of voids at the CuO-Zr and Zr-CuO interfaces.

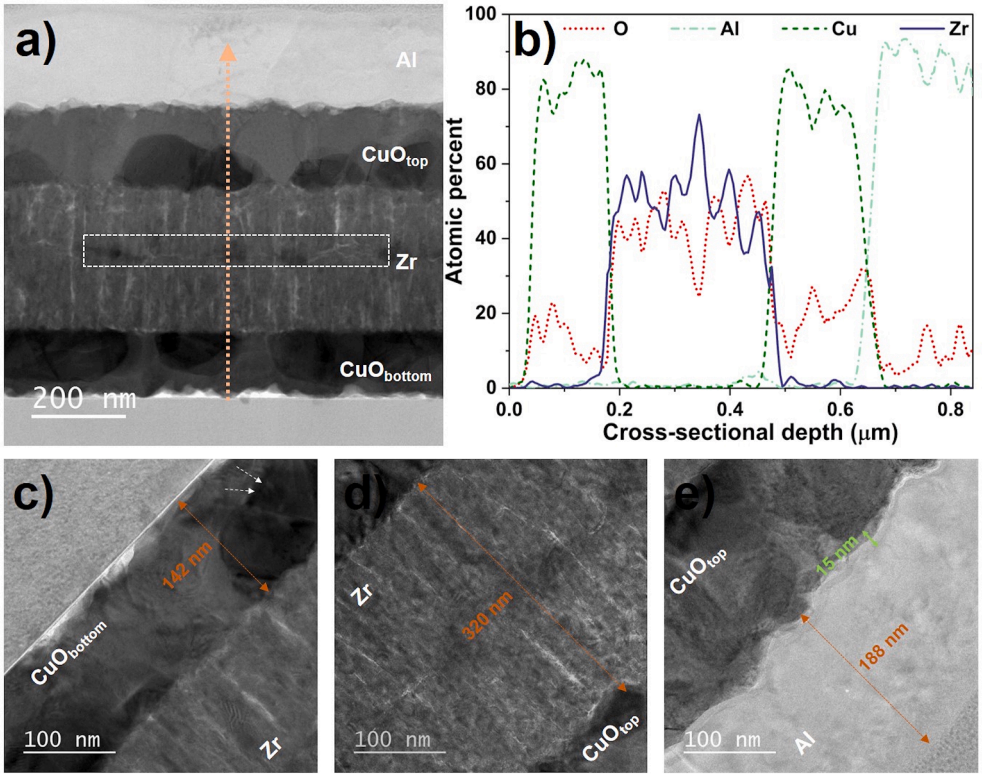

Fig. 4. Microstructural evolution post-annealing at 375 °C is depicted, showing: **a)** STEM micrograph of the CuO-Zr-CuO-Al system, and **b)** corresponding EDX quantification of O, Cu, Al, and Zr. The dotted rectangular area in (a) is Zr-rich (O deficient). TEM micrographs of each of the three interfaces are presented: **c)** CuO-Zr, **d)** Zr-CuO, and **e)** CuO-Al. The white dotted arrows indicate the large Cu grains in (c) formed as a result of CuO reduction.

Al.

Complete Zr oxidation: The STEM micrograph, corresponding ascending EDX profile as well as the TEM images of the three interfaces of CuO-Zr-CuO-Al annealed at 450 °C are shown in Fig. 5. This temperature marks the end of Zr/CuO exothermic reaction. Most of the bottom and top CuO nanolayer is populated with micron sized grains of metallic Cu. The average layer thicknesses were measured at locations of a continuous CuO availability, and the bottom and the top CuO depreciate by ~46% and 25% respectively compared to the initial thickness. Given the final microstructure (Fig. 5**a**), these decrements fail to give an accurate picture of CuO consumption. The XRD on the other hand, did not show the presence of any CuO at 450 °C, but recorded Cu signals, indicating a full reduction. This is further confirmed by the EDX quantitative analysis (Fig. 5**b**) wherein no oxygen is detected in the CuO layer, except in the vicinity of the CuO-Al interface.

The oxidized Zr layer expands to approximately 340 ± 5.2 nm, representing a final growth of roughly 53% compared to its initial thickness. As oxygen ions migrate deeper into the Zr layer from the interfaces, the lattice of Zr expands, leading to the development of internal stresses within the ZrO_x layer. These stresses, combined with the high Pilling-Bedworth ratio of Zr (1.56), contribute to the formation of multiple cracks within the layer (darker regions, Fig. 5**d**). Additionally, as ZrO_x undergoes oxidation, the oxidized Zr layer exhibits a granular morphology, transitioning towards a more stable zirconia phase. In Fig. 5**b**, Zr and O signals display a greater degree of overlap with average atomic percent at 45 and 55% respectively compared to the partial Zr oxidation scenario. Additionally, an EDX quantification on zirconia results in Zr-O atomic ratio of 40:60 (**Figure S15**). This substantiates the presence of zirconia, although further qualitative assessment through EELS is required to strongly argue its presence. The dotted regions vertically halfway through the multilayer **(**Fig. 5**d)** indicate a region of higher density than the surrounding zirconia layer. The thickness of this region was too low to accurately identify the material using EDX depth profile. However, upon mapping each of the three elements, O, Cu and Zr, as shown in **Figure S16**, a clear presence of Cu was detected within zirconia. This phenomenon occurs as zirconia expands into the CuO matrix, subsequently trapping Cu within its structure while consuming oxygen from CuO. Additionally, the presence of Cu halfway in the zirconia layer comes from the migration of Cu atoms through the porous zirconia, originating from both the CuO-Zr and Zr-CuO interfaces.

The Al layer reduces to 177 ± 12.8 nm, exhibiting a 12% reduction in its thickness. The first Al/CuO exotherm is centered at ~450 °C, which marks the Al-O diffusion across the interface until the interface is thick enough to inhibit any further O diffusion through a thick amorphous alumina. The decrease in Al thickness is attributed to its expansion through solid-state diffusion at this temperature. As seen in the EDX profile, most of the oxygen in the Al layer is concentrated at the interface only supporting this chemical regime.

The CuO-Zr and Zr-CuO interfaces (Fig. 5**c-d**) appear to be continuous. The sharp transition at both interfaces made it difficult to obtain the interfacial thicknesses. Unlike the low temperature mass transport scenario, the metallic Cu grains (dotted arrows, Fig. 5**c**) grow large enough to fill any voids and form a dense interface junction on both ends of the Zr layer. The CuO-Al interface appears severely damaged decorated with several voids. The observed behavior deviates from what was reported in a previous paper on Al only system [5], leading us to speculate that the damage might result from the reaction of the majority of the upper CuO layer with Zr, causing it to detach from the CuO-Al interface. This leads to a much thicker CuO-Al interface of 48 ± 4.4 nm.

In summary, EDX analysis conducted across the three reaction regimes of preliminary mass transport, partial Zr oxidation, and complete Zr oxidation offers chemical quantification and valuable insights into the chemical transformation occurring within each of the three nanolayers: CuO, Zr, and Al, as they engage in the reaction process.

While it aids in addressing most inquiries regarding solid-state diffusion, it does not provide conclusive evidence regarding the

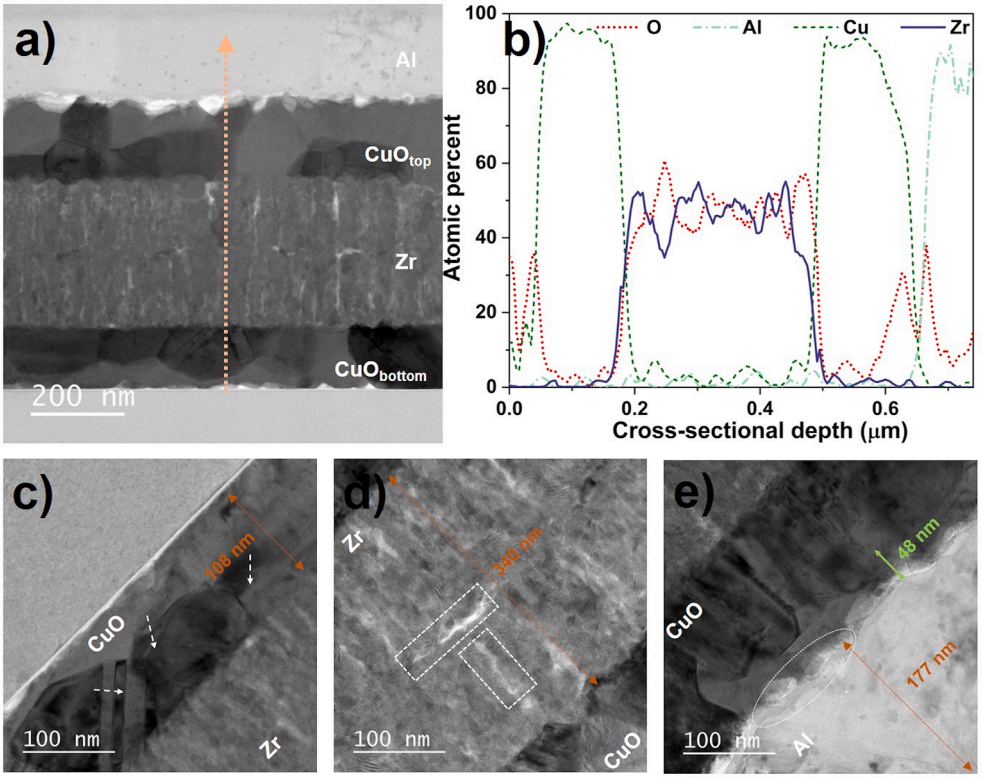

Fig. 5. Microstructural evolution following annealing at 450 °C, featuring: **a)** STEM micrograph of the CuO-Zr-CuO-Al system and **b)** corresponding EDX quantification of O, Cu, Al, and Zr. TEM micrographs showcasing each of the three interfaces: **c)** CuO-Zr, **d)** Zr-CuO, and **e)** CuO-Al. The white dotted arrows highlight large Cu grains in (c), dotted rectangular regions denote diffused Cu in Zr in (d), and the circular area in (e) indicates damage to the CuO-Al interface.

oxidation state of Zr. Hence, as a concluding experiment, HAADF imaging was conducted on the Zr layer, coupled with EELS to examine the progression of oxidation states within the Zr layer, focusing on the Energy Loss Near Edge Structures (ELNES) of Zr-$L_{2,3}$ and O-K edges. Additionally, the low-loss edges of Zr ($N_{2,3}$) were also captured to discern the existence of Zr^{2+} and Zr^{4+}.

3.4. Progression of Zr oxidation

Fig. 6 shows the microstructural evolution of Zr layer as a function of temperature. Partial oxidation becomes evident when the temperature reaches 375 °C, resulting in Zr-rich regions in the middle of the layer. Complete oxidation occurs at 450 °C, where all Zr is oxidized to ZrO_2. The increase in thickness of the Zr layer from its initial 220 nm to approximately 340 nm corresponds to a change by a factor of 1.54. This closely matches the Pilling-Bedworth ratio of 1.56, indicating that theoretically, the volume occupied by zirconia should expand by 1.56 times upon oxidation. Albeit it doesn't account for lateral expansion, the observed expansion aligns well with the expected theoretical outcome. Fig. 7 illustrates the change in the chemical profile throughout the layer in a magnified view. The subsequent step involves determining the oxidation states of Zr to understand the sequential reaction steps.

ELNES of O, Cu and Zr for ZrO_x layer annealed at the three temperatures of 275 °C, 375 °C and 450 °C are shown in Fig. 8**a-c**. Additionally, $N_{2,3}$ edges of Zr were also recorded at some locations within the Zr layer. Fig. 6**a-c** indicate the locations of each point from where an EELS spectrum was collected. Typically, a splitting of the 4d orbital in Zr results in two subdivided L_2 peaks in Zr at 2222 eV [28]. However, the presence of L edges at such a high energy render it difficult to observe the splitting with a typical 1 eV spatial resolution and reasonable acquisition times. Thus, it is not uncommon to not observe the peak splitting. In addition, $L_{2,3}$ edges are characterized by a 2.45 eV shift when the oxidation state changes from 0 to + 4 [29], which is difficult to observe in a standard EELS experiment. Here, we utilize the $N_{2,3}$ low-energy loss edges of Zr to examine the evolution of the oxidation states. Due to the extensive range of desired energy spectra, these measurements are selectively recorded at specific locations as indicated by the white dotted arrow in Fig. 6.

When annealed at 275 °C (Fig. 8**a**), the Zr layer can be divided into three regions. The O K-edge at 532 eV is recorded only at the extremities of the Zr layer with no clear detection in the middle of the layer. This contradicts the presence of oxygen detected using EDX, suggesting that it may be attributable to background noise or non-uniform distribution of oxygen. As for Zr, the $L_{2,3}$ ELNES are detected at 2307–2222 eV with no apparent shift through the entirety of the layer. However, the ratio of the intensity of L_3:L_2 increases, which is an indication of shift of Zr metal to oxidized Zr (ZrO, ZrO_2) as reported previously [29]. This increase is noticed at both top and bottom ends of the Zr layer, unlike in the middle. Moreover, the observation of $N_{2,3}$ edges at approximately 28 eV at both the top and bottom of the oxidized Zr layer serves as additional confirmation of the oxidation state of Zr being at + 4 [29,30]. The incidence of a shoulder in the 15-eV edge supports the formation of ZrO [29], also detected weakly in the XRD. Other signals however strongly indicate towards either 0 or + 4 oxidation states of Zr only. This corroborates the elemental quantification, providing further evidence for the initiation of zirconia formation.

Increasing the temperature to 375 °C results in further oxidation of Zr to ZrO and ZrO_2. Unlike the middle region, the presence of $N_{2,3}$ Zr edges at 28 eV support this claim. The absence of a gradual decreasing shoulder or peak broadening however indicate towards no ZrO formation. The presence of oxygen detected during EDX quantification, surpassing the 10% detection limit, suggests that Zr is saturated with oxygen. This saturation results in a similar signature to that of pure Zr metal [29]. Therefore, although it would be challenging to distinguish between Zr in its metallic state (oxidation state of 0) and oxygen-saturated Zr (with oxidation state between 0 and + 4) based on the low loss edges, the microstructural changes and EDX mapping strongly suggest a higher likelihood of oxygen enriched Zr. The Zr $L_{2,3}$ edges exhibit a similar change in the intensity ratios as seen in the 275 °C-annealed sample, corroborating the inward growth of zirconia via oxygen diffusion. Interestingly, the O K-edge in the bottom region of zirconia displays some splitting, consistent with the occurrence of + 4 oxidation state of Zr as oppose to 0 or + 2 [29]. No Cu was detected anywhere throughout the ZrO_x layer.

At the conclusion of all exothermic events at ~450 °C, Fig. 8**c** displays the Zr $N_{2,3}$ and $L_{2,3}$ ELNES. Unsurprisingly, the $L_{2,3}$ peak intensity ratios do not show a significant change. This indicates the presence of a single-phase material. Additionally, the low loss edges are characterized by identifying $N_{2,3}$ edges at 16 and 28 eV confirming the + 4-oxidation state of Zr (**Figure S17**). The splitting of O K-edge also provide backing to this claim. Another noteworthy feature is the detection of weak $L_{2,3}$ edges of Cu at ~931 eV, which in fact supports the prior EDX analysis showing significant Cu diffusion into the crevices of zirconia.

Unlike Al/CuO thermite couple, wherein the occurrence of a pre-peak indicating the presence of molecular oxygen is commonly observed [20,22], no such detection was observed here. This comes as a direct result of higher oxygen diffusivity in zirconia against alumina. Consequently, this leads to the rapid reduction of CuO to Cu, with some intermediate Cu_2O formation. Cu_2O was not detected by EELS (**Figure S18**), despite XRD showing some Cu_2O-related signals (Table 1). This discrepancy may be due to the insignificant presence of Cu_2O at the interface by the time the sample was characterized by EELS. Thus, although Cu_2O forms, it is not always detectable at equilibrium. The weak presence of Cu_2O at the low temperature of 275 °C is indicative of a preliminary metastable state, which rapidly converts to metallic Cu at the interface.

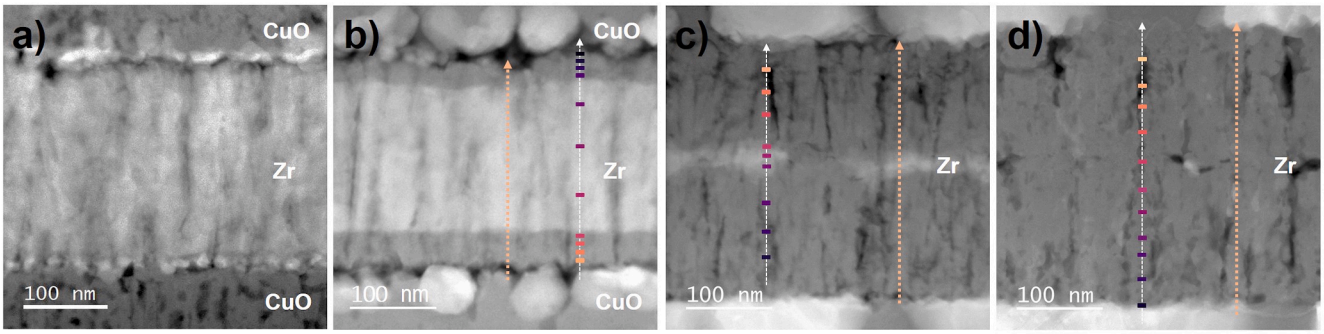

Fig. 6. STEM micrograph showing the annealed Zr layer at temperatures **a)** 25 °C, **b)** 275 °C, **c)** 375 °C and **d)** 450 °C. Scans are recorded in a bottom-to-top sequence. The orange arrow indicates the location of EDX scan averaged over an area (Fig. 7). The white arrow indicates the position of each point where an EELS scan was performed (Fig. 8). (For interpretation of the references to colour in this figure legend, the reader is referred to the web version of this article.)

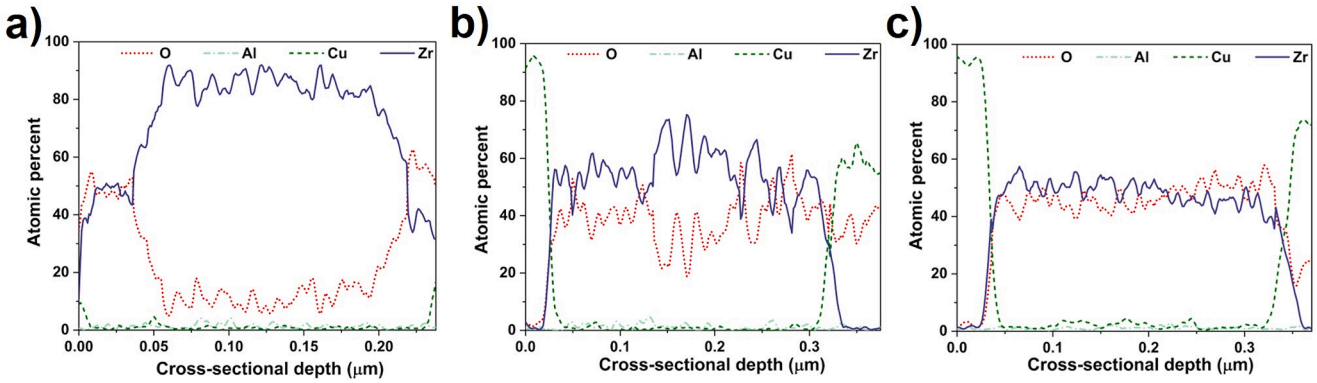

Fig. 7. Quantitative EDX analysis of the Zr layer annealed at temperatures **a)** 275 °C, **b)** 375 °C, and **c)** 450 °C.

3.5. Reaction mechanism

By employing STEM-EELS alongside EDX and XRD, conclusive evidence was obtained supporting the presence of three oxidation states of Zr: 0 (metallic), +4 (zirconia), and an intermediate state between 0 and + 4 (ZrO or oxygen-enriched Zr). In addition and unlike Al/CuO thermite system wherein CuO decomposition is first observed at ~350 °C [22], CuO decomposition was seen as early as 275 °C. With minor Cu_2O detection, it is deduced that CuO even though decomposing to form Cu_2O suboxide, continues to degrade to Cu while oxidizing zirconia in the process. This is in agreement with a higher Zr-O bond dissociation energy (760 kJ.mol^{-1}) than that of Cu-O (343 kJ.mol^{-1}). The initial detection of metallic Cu at 375 °C, as observed by XRD, supports the assertion of a complete reaction pathway from CuO to Cu. Thus, the sequential reactions can be summarized as follows:

Step I: 275 °C	2 CuO (s) → Cu_2O (s) + O (s)
	Cu_2O (s) + O (s) → 2 Cu (s) + 2O (s)Zr
	(s) + O (s) → ZrO (s)
Step II: 375 °C	ZrO (s) + O (s) → ZrO_2 (s) CuO
	(s) → Cu (s) + O (s)
Step III: 450 °C	Zr (s) + 2O (s) → ZrO_2 (s)

In contrast to the behavior observed in Al/CuO systems [22], there is no evidence of alloy formation between Cu and Zr, despite the notable presence of Cu within the zirconia layer. Additionally, the slow diffusion kinetics of Al and O are surpassed by the rapid oxygen scavenging ability of Zr, leading to aggressive oxidation at lower temperatures. This highlights the superiority of Zr as a fuel, as it undergoes oxidation in the condensed phase, unlike Al where oxidation primarily occurs in the vapor and condensed phases. Furthermore, despite a higher standard reduction potential of Al (-1.66 V) [31] compared to Zr (-1.53 V) [32], the latter's reactivity is relatively superior.

Regarding the microstructural alterations stemming from the chemical reactions, Fig. 9 illustrates the reaction progression from lower to higher temperatures. Initially, heating triggers oxygen diffusion, leading to the formation of oxide scales near the interfaces. Consequently, the Zr layer separates from the CuO surface, with the voids being filled by oxygen. This oxygen is then consumed by the Zr layer as the scales expand vertically and laterally. The grain growth persists until all of the Zr is transformed into zirconia, resulting in dense Cu-ZrO_2 interfaces.

3.6. Performance of Zr as a fuel: Ignition and combustion

As a concluding experiment, intended to showcase the enhanced energetic performance of Zr compared to Al as a fuel, Zr/CuO exhibited an autoignition temperature of 335 ± 5 °C, while the extremely low reactivity of the Al counterpart was evident with a high ignition point of 790 ± 10 °C (Fig. 10). The glass wafer hot point ignition tests revealed that the 3 BL Zr/CuO multilayer achieved a 100% ignition success rate, with an average ignition delay time of 0.04 ± 0.016 ms. The average ignition energy recorded for Zr/CuO was 0.2 ± 0.14 mJ. The 3 BL Al/CuO sample failed to ignite, which is primarily attributed to its notably low reactivity, compounded by insufficient material presence and significant thermal losses. As for the propagation rates, whereas 3 BL Al/CuO failed to propagate, Zr/CuO demonstrated a self-sustained propagation at a rate of 3.5 ± 0.10 m.s^{-1}. The presence of less material, low oxygen diffusivity in alumina and higher thermal losses to the environment collectively resulted in lower self-sustenance of Al/CuO reaction. The rapid oxygen exchange reaction between Zr and CuO as well as a massively higher oxygen diffusivity [16] through ZrO_2 at similar temperatures underwrites a greater reaction volume and heat of reaction, thus exhibiting much lower ignition delay time. Zr, both as a fuel and an additive in the development of a ternary nanolaminate system, can therefore enhance the overall energetic performance, particularly in scenarios where shorter ignition delay times and significant energy release over shorter durations are sought after.

4. Conclusion

Nanoscale reactive multilayer films were fabricated using magnetron sputtering using CuO as the source of oxygen and investigating the physio-chemical processes involving Zr. Unlike Al/CuO, the reactivity of Zr/CuO thermite system was found to be highly dependent on the transport properties of the terminal oxide generated during the chemical reaction. Thermo-physical analysis, employing both DSC and XRD of the annealed samples, was performed to validate this correlation. In contrast to the 5% release observed in Al/CuO, Zr/CuO thermite liberates 100% of its total heat below 500 °C. Furthermore, while Al experiences an initial Al-O dual diffusion, leading to the formation of amorphous alumina, Zr begins producing the terminal reaction product at temperatures as low as 275 °C due to Zr oxidation occurring in the condensed phase only. The partially reacted Zr/CuO RMFs were subsequently imaged and spectroscopically characterized using atomically resolved STEM-HAADF and EDX. In addition, EELS in STEM mode as well as low loss EELS were utilized to track the oxidation states during the sequential stages of the reaction. The investigation reveals that CuO undergoes a one-step reduction process to Cu, while simultaneously oxidizing Zr. The oxidation of Zr, resulting in the formation of both ZrO_x and ZrO_2 simultaneously, undergoes a subsequent oxidation process at ~375 °C that is characterized by a higher heat release and grain growth. From this temperature onward, all Zr and oxygen-enriched Zr (oxide scales) are completely converted to ZrO_2. Furthermore, unlike the formation of Al-Cu alloy, which depletes the Al fuel prior to the thermite reaction, no alloying between Cu and Zr was observed. Finally, against the inability of 3 BL Al/CuO to ignite, 3 BL Zr/CuO exhibited 100% ignition success with an ignition delay time of 0.04 ± 0.016 ms. In comparison to Al/CuO, Zr/CuO demonstrated success in sustaining the

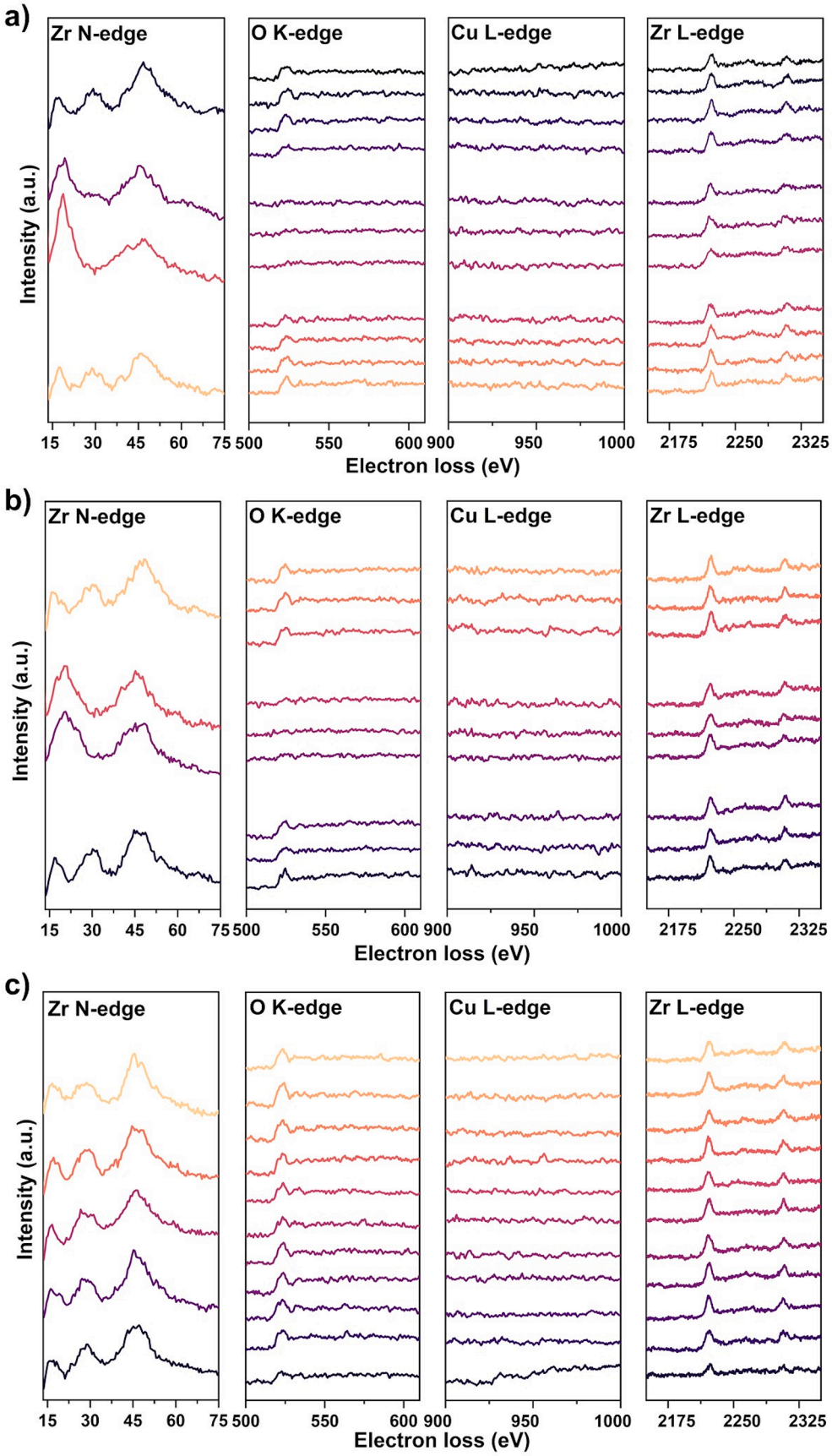

Fig. 8. EELS analysis of Zr layer annealed at temperatures **a)** 275 °C, **b)** 375 °C, and **c)** 450 °C. The $N_{2\text{-}3}$ edges of Zr are recorded at specific positions to distinguish the Zr^{4+}oxidation state.

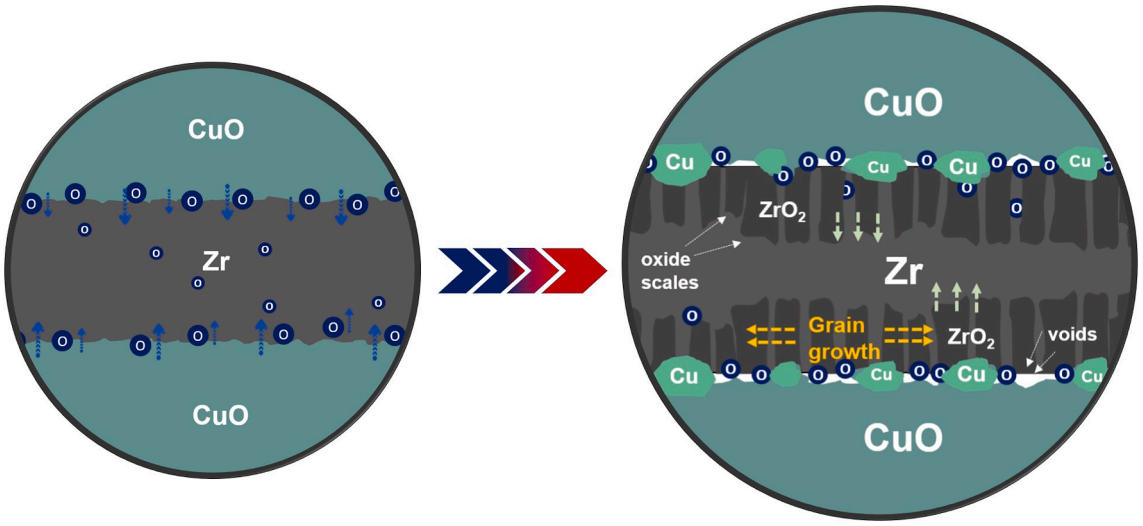

Fig. 9. A simplified schematic depicting the microstructural evolution of the Zr layer. The oxidation process, facilitated by outward oxygen migration, leads to the formation of columnar structures within the Zr layer. Subsequent oxidation results in the expansion of these structures into larger grains.

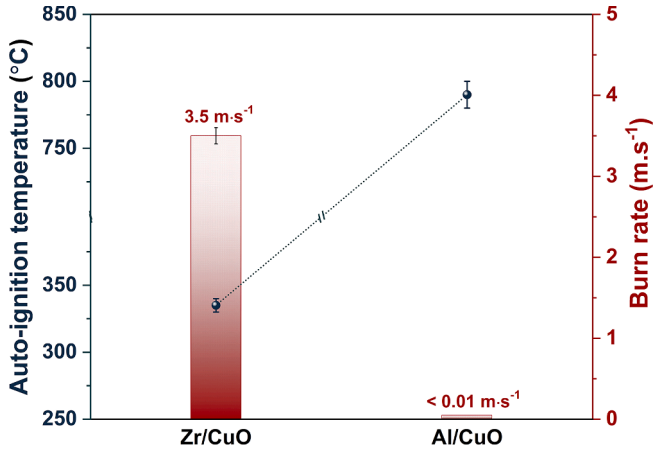

Fig. 10. Auto-ignition temperature and burn rate of Zr and Al as fuels coupled with CuO oxidizer.

combustion reaction. These properties therefore emphasize the exceptional suitability of Zr as a thermite fuel.

Funding sources

C.R. received funding from the European Research Council (ERC) under the European Union's Horizon 2020 research and innovation program (grand agreement No. 832,889 – PyroSafe).

CRediT authorship contribution statement

Vidushi Singh: Conceptualization, Methodology, Investigation, Formal analysis, Data curation, Visualization, Validation, Writing – original draft, Writing – review & editing. **Tao Wu:** Visualization, Validation, Writing – review & editing. **Christophe Tenailleau:** Validation, Resources, Writing – review & editing. **Teresa Hungria:** Validation, Writing – review & editing. **Alain Estève:** Validation, Supervision, Writing – review & editing, Project administration. **Carole Rossi:** Conceptualization, Methodology, Validation, Resources, Supervision, Writing – review & editing, Project administration, Funding acquisition.

Declaration of competing interest

The authors declare that they have no known competing financial interests or personal relationships that could have appeared to influence the work reported in this paper.

Data availability

No data was used for the research described in the article.

Acknowledgements

The authors gratefully acknowledge the support from the European Research Council (H2020 Excellent Science) Researcher Award (grant 832889 – PyroSafe). This work was also supported by LAAS-CNRS technology platform, a member of Renatech network.

Appendix A. Supplementary data

Supplementary data to this article can be found online at https://doi.org/10.1016/j.cej.2024.153357.

References

[1] C. Rossi, Metallized reactive materials – a road to clean and sustainable pyrotechnics, Propell. Explos. Pyrotech. 48 (2023) e202380531.
[2] G.C.S. Freitas, F.C. Peixoto, A.S. Vianna, Simulation of a thermal battery using Phoenics®, J. Power Sources 179 (2008) 424–429, https://doi.org/10.1016/j.jpowsour.2007.11.084.
[3] H. Habu, M. Okada, M. Ito, K. Nozoe, T. Kawano, S. Matsumoto, Y. Yoshida, Thermite as a chemical heat source for the science payload, Sci. Tech. Energetic Materials 73 (2012) 5.
[4] From chips to dust: The MEMS shatter secure chip | IEEE Conference Publication | IEEE Xplore, (n.d.). https://ieeexplore.ieee.org/document/6765843 (accessed April 22, 2024).
[5] F. Sevely, T. Wu, F.S. Ferreira de Sousa, L. Seguier, V. Brossa, S. Charlot, A. Esteve, C. Rossi, Developing a highly responsive miniaturized security device based on a printed copper ammine energetic composite, Sens. Actuators, A 346 (2022) 113838, https://doi.org/10.1016/j.sna.2022.113838.
[6] O. Odawara, T. Fujita, A.V. Gubarevich, H. Wada, Thermite-related technologies for use in extreme geothermal environments, Int. J. Self Propag. High Temp. Synth. 27 (2018) 228–235, https://doi.org/10.3103/S1061386218040040.
[7] T. Wu, G. Lahiner, C. Tenailleau, B. Reig, T. Hungría, A. Estève, C. Rossi, Unexpected enhanced reactivity of aluminized nanothermites by accelerated aging, Chem. Eng. J. 418 (2021) 129432, https://doi.org/10.1016/j.cej.2021.129432.
[8] E.L. Dreizin, Metal-based reactive nanomaterials, Prog. Energy Combust. Sci. 35 (2) (2009) 141–167, https://doi.org/10.1016/j.pecs.2008.09.001.
[9] J.P. Abriata, J. Garcés, R. Versaci, The O–Zr (Oxygen-Zirconium) system, Bull. Alloy Phase Diagr. 7 (1986) 116–124, https://doi.org/10.1007/BF02881546.

[10] B.S. Min, H.S. Hyun, Study on combustion characteristics and performance of HTPB/AP propellants containing zirconium, J. Propul. Power 28 (2012) 211–213, https://doi.org/10.2514/1.B34120.
[11] C. Badiola, E.L. Dreizin, Combustion of micron-sized particles of titanium and zirconium, Proc. Combust. Inst. 34 (2013) 2237–2243, https://doi.org/10.1016/j.proci.2012.05.089.
[12] W.D. Bates, C. Gotzmer, Development of passivated pyrophoric metal powders (hafnium and zirconium) with reduced electrostatic discharge (ESD) sensitivity, IJEMCP 5 (2002), https://doi.org/10.1615/IntJEnergeticMaterialsChemProp.v5.i1-6.1000.
[13] B. Lv, Y. Xu, B. Hou, D. Wu, Y. Sun, Preparation and combustion properties of α-Fe2O3 coated Zr particles, Mater. Res. Bull. 43 (2008) 2769–2777, https://doi.org/10.1016/j.materresbull.2007.10.022.
[14] Q. Wang, J. Sun, J. Deng, H. Wen, Y. Xu, Combustion Behaviour of Fe2O3-coated Zirconium Particles in Air, Energy Procedia 66 (2015) 269–272, https://doi.org/10.1016/j.egypro.2015.02.053.
[15] C. Woodruff, E.R. Wainwright, S. Bhattacharia, S.V. Lakshman, T.P. Weihs, M. L. Pantoya, Thermite reactivity with ball milled aluminum-zirconium fuel particles, Combust. Flame 211 (2020) 195–201, https://doi.org/10.1016/j.combustflame.2019.09.028.
[16] E.J. Mily, A. Oni, J.M. Lebeau, Y. Liu, H.J. Brown-Shaklee, J.F. Ihlefeld, J.-P. Maria, The role of terminal oxide structure and properties in nanothermite reactions, Thin Solid Films 562 (2014) 405–410, https://doi.org/10.1016/j.tsf.2014.05.005.
[17] H. Jabraoui, A. Esteve, M. Schoenitz, E.L. Dreizin, C. Rossi, Atomic scale insights into the first reaction stages prior to Al/CuO nanothermite ignition: influence of porosity, ACS Appl. Mater. Interfaces 14 (2022) 29451–29461, https://doi.org/10.1021/acsami.2c07069.
[18] V. Singh, T. Wu, E. Hagen, L. Salvagnac, C. Tenailleau, A. Estéve, M.R. Zachariah, C. Rossi, How positioning of a hard ceramic TiB2 layer in Al/CuO multilayers can regulate the overall energy release behavior, Fuel 349 (2023) 128599, https://doi.org/10.1016/j.fuel.2023.128599.
[19] V. Singh, T. Wu, L. Salvagnac, A. Estève, C. Rossi, Ignition and combustion characteristics of Al/TiB2-based nanothermites: effect of bifuel distribution, ACS Appl. Nano Mater. (2024), https://doi.org/10.1021/acsanm.3c05578.
[20] T. Wu, V. Singh, B. Julien, C. Tenailleau, A. Estève, C. Rossi, Pioneering insights into the superior performance of titanium as a fuel in energetic materials, Chem. Eng. J. 453 (2023) 139922, https://doi.org/10.1016/j.cej.2022.139922.
[21] Transmission Electron Microscopy and Diffractometry of Materials, Springer, Berlin, Heidelberg, 2008. https://doi.org/10.1007/978-3-540-73886-2.
[22] V. Singh, B. Julien, L. Salvagnac, S. Pelloquin, T. Hungria, C. Josse, M. Belhaj, C. Rossi, Influence of process parameters on energetic properties of sputter-deposited Al/CuO reactive multilayers, Nanotechnology (2022), https://doi.org/10.1088/1361-6528/ac85c5.
[23] Y. Wang, J. Ghanbaja, F. Soldera, S. Migot, P. Boulet, D. Horwat, F. Mücklich, J. F. Pierson, Tuning the structure and preferred orientation in reactively sputtered copper oxide thin films, Appl. Surf. Sci. 335 (2015) 85–91, https://doi.org/10.1016/j.apsusc.2015.02.028.
[24] K. Khojier, H. Savaloni, F. Jafari, Structural, electrical, and decorative properties of sputtered zirconium thin films during post-annealing process, J. Theor. Appl. Phys. 7 (2013) 55, https://doi.org/10.1186/2251-7235-7-55.
[25] Y. Wang, S. Lany, J. Ghanbaja, Y. Fagot-Revurat, Y.P. Chen, F. Soldera, D. Horwat, F. Mücklich, J.F. Pierson, Electronic structures of C u 2 O, C u 4 O 3, and CuO: A joint experimental and theoretical study, Phys. Rev. B 94 (2016) 245418, https://doi.org/10.1103/PhysRevB.94.245418.
[26] J. Li, J.W. Mayer, Oxidation and reduction of copper oxide thin films, Mater. Chem. Phys. 32 (1992) 1–24, https://doi.org/10.1016/0254-0584(92)90243-2.
[27] I. Abdallah, J. Zapata, G. Lahiner, B. Warot-Fonrose, J. Cure, Y. Chabal, A. Esteve, C. Rossi, Structure and chemical characterization at the atomic level of reactions in Al/CuO multilayers, ACS Appl. Energy Mater. 1 (2018) 1762–1770, https://doi.org/10.1021/acsaem.8b00296.
[28] N. Thromat, C. Noguera, M. Gautier, F. Jollet, J.P. Duraud, Electronic structure and atomic arrangement around Zr substituted for Y in ${\mathrm{Y}}_{2}$ ${\mathrm{O}}_{3}$, Phys. Rev. B 44 (1991) 7904–7911, https://doi.org/10.1103/PhysRevB.44.7904.
[29] K.J. Annand, I. MacLaren, M. Gass, Utilising Dual EELS to probe the nanoscale mechanisms of the corrosion of Zircaloy-4 in 350 °C pressurised water, J. Nucl. Mater. 465 (2015) 390–399, https://doi.org/10.1016/j.jnucmat.2015.06.022.
[30] S.K. Dey, C.-G. Wang, D. Tang, M.J. Kim, R.W. Carpenter, C. Werkhoven, E. Shero, Atomic layer chemical vapor deposition of ZrO2-based dielectric films: Nanostructure and nanochemistry, J. Appl. Phys. 93 (2003) 4144–4415, https://doi.org/10.1063/1.1555257.
[31] W. Li, T. Cochell, A. Manthiram, Activation of aluminum as an effective reducing agent by pitting corrosion for wet-chemical synthesis, Sci. Rep. 3 (2013) 1229, https://doi.org/10.1038/srep01229.
[32] T.-L. Yau, V.E. Annamalai, Corrosion of Zirconium and its Alloys. Reference Module in Materials Science and Materials Engineering, Elsevier, 2016, 10.1016/B978-0-12-803581-8.09220-1.